nature communications

Article

https://doi.org/10.1038/s41467-024-53833-x

Lattice hydrogen transfer in titanium hydride enhances electrocatalytic nitrate to ammonia conversion

Received: 23 May 2024

Accepted: 23 October 2024

Published online: 03 November 2024

Check for updates

Jiawei Li[1], Wanqiang Yu[1], Haifeng Yuan[1], Yujie Wang[1], Yuke Chen[1], Di Jiang[1], Tong Wu[1], Kepeng Song[2], Xuchuan Jiang[3], Hong Liu[1,4], Riming Hu[3] ✉, Man Huang[1] ✉ & Weijia Zhou[1] ✉

The electrocatalytic reduction of nitrate toward ammonia under mild conditions addresses many challenges of the Haber-Bosch reaction, providing a sustainable method for ammonia synthesis, yet it is limited by sluggish reduction kinetics and multiple competing reactions. Here, the titanium hydride electrocatalyst is synthesized by electrochemical hydrogenation reconstruction of titanium fiber paper, which achieves a large ammonia yield rate of 83.64 mg h^{-1} cm^{-2} and a high Faradaic efficiency of 99.11% with an ampere-level current density of 1.05 A cm^{-2} at −0.7 V versus the reversible hydrogen electrode. Electrochemical evaluation and kinetic studies indicate that the lattice hydrogen transfer from titanium hydride promotes the electrocatalytic performance of nitrate reduction reaction and the reversible equilibrium reaction between lattice hydrogen and activate hydrogen not only improves the electrocatalytic activity of nitrate reduction reaction but also demonstrates notable catalytic stability. These finding offers a universal design principle for metal hydrides as catalysts for effectively electrochemical ammonia production, highlighting their potential for sustainable ammonia synthesis.

Ammonia (NH_3) is an important chemical commonly used in agriculture, plastics, pharmaceuticals, and other industries[1–4]. The Haber-Bosch process supplied humans and crops with NH_3, contributing significantly to human development for over a century[5,6]. However, the Haber-Bosch reaction required rigorous conditions, including temperatures (~500 °C) and pressures (>100 atm), to initiate the slow reaction of N_2 and H_2[7–9]. To achieve carbon neutrality and address the global energy crisis, it was vital to explore a green and energy-efficient process for NH_3 synthesis. Nitrogen gas (N_2) from air has been recognized as a key nitrogen contributor for a promising approach through the electrochemical nitrogen reduction reaction (NRR)[10]. However, the challenge with NRR laid in the remarkably stable N ≡ N bonds (941 kJ mol^{-1}) and its limited solubility in water[11], which led to poor selectivity and low efficiency in the reaction[12,13].

In contrast, the transformation of nitrate (NO_3^-) into NH_3 via the nitrate reduction reaction (NIRR) could circumvent the issue of N_2's solubility in water. The NO_3^- was particularly active since it possessed low N = O bond cleavage energy (204 kJ mol^{-1})[14,15]. Direct synthesis of NH_3 from NO_3^- could potentially reduce water pollution, conserve energy, and promote sustainable NH_3 production[16]. Moreover, converting high concentrations of NO_3^- to NH_3 was significant for both environmental and energy considerations[17]. From an environmental perspective, high-concentration nitrate waste waters typically come from sources like landfill leachate, aquaculture wastewater, and the

[1]Institute for Advanced Interdisciplinary Research (iAIR), School of Chemistry and Chemical Engineering, University of Jinan, Jinan, P. R. China. [2]Electron Microscopy Center, Shandong University, Jinan, Shandong, P. R. China. [3]Institute for Smart Materials & Engineering, University of Jinan, Jinan, P. R. China. [4]State Key Laboratory of Crystal Materials, Shandong University, Jinan, Shandong, P. R. China. ✉e-mail: ism_hurm@ujn.edu.cn; ifc_huangm@ujn.edu.cn; ifc_zhouwj@ujn.edu.cn

fertilizer industry. From an energy perspective, reducing high-concentration nitrates to synthesize NH_3 could generate a significant amount of NH_3, making the recovery of NH_3 worthwhile. Nonetheless, the process of converting NO_3^- to NH_3 involved a complex reaction requiring the transfer of 8 electrons and 9 protons ($NO_3^- + 6H_2O + 8e^- \rightarrow NH_3 + 9OH^-, PH = 14$), with numerous potential intermediates[5,18]. The competitive hydrogen evolution reaction (HER) and various by-products complicate the reaction pathways, reducing the selectivity and efficiency of NIRR[19,20], which needed an efficient electrocatalyst for NIRR.

In order to rationally design NIRR catalysts, an in-depth mechanistic understanding of the reaction was necessary. Conventional strategy is generally needed to design tandem catalysts that possess both nitrate activation sites and hydrogenation sites to achieve high nitrate catalytic activity. For example, in our team's previous research, laser-controlled preparation of CuNi alloy as nitrate reduction electrocatalyst with tandem catalytic sites[17]. The active hydrogen (H*) in the hydrogenation reaction typically comes from water in the electrolyte. If there was insufficient active hydrogen available for the NIRR, it would limit the efficiency of converting NO_3^- to NH_3. Thus, designing an in situ hydrogenation reaction on the electrocatalyst to improve the NIRR efficiency remains an area that requires further research.

In general, titanium hydride has attracted attention for its ability as a hydrogen storage material[21,22]. Thomas F. Jaramillo employed titanium metal as the electrode for efficient electrochemical nitrate reduction to ammonia[23]. During the NIRR process, the titanium hydride was detected after long-time catalysis, but the contribution of titanium metal and titanium hydrides to the catalysis could not be determined. In addition, other hydrogenation phenomena had also been observed in the electrochemical reduction of nitrate[24,25]. Further, William A. Tarpeh reported that titanium hydrides exhibited excellent nitrate-catalytic activity and investigated the catalyst structure in detail using GIXRD and XAS. They highlighted the significance of connecting NIRR performance to the near-surface electrode structure to improve catalyst design and operation[26]. However, they believed that the reason for the high catalytic activity of hydrogenated titanium was attributed to the traditional proton-transfer mechanism (H* was derived from the electrolyte). So, the mechanism of lattice hydrogen participating in the hydrogenation catalytic reaction has not been proposed and confirmed.

In this work, the titanium hydride electrocatalyst is synthesized by electrochemical hydrogenation reconstruction of titanium fiber paper (Ti FP). The obtained titanium hydride electrocatalyst exhibited a high NH_3 yield rate of 83.64 mg h^{-1} cm^{-2} and Faradaic efficiency (FE) of 99.11% along with the ampere-level current density of 1.05 A cm^{-2} at − 0.7 V versus the reversible hydrogen electrode (RHE). We confirmed the hydrogenation reaction involving lattice hydrogen during the NIRR process through isotopic tracking experiments and theoretical calculations. The lattice hydrogen transfer mechanism was proposed, and the reversible equilibrium reaction between lattice hydrogen and active hydrogen (H*) was confirmed to not only improve the electrocatalytic activity of NIRR but also demonstrate high catalytic stability. The more important matter was that the proposed mechanism of lattice hydrogen participating in the reversible catalytic reaction could be extended to other metal hydrides, such as palladium hydride, tantalum hydride, and vanadium hydride. This understanding provided a universal design concept for metal hydrides as catalysts and lattice hydrogen as H* sources for efficient electrochemical NH_3 production, highlighting their potential for sustainable ammonia synthesis.

Results

Preparation and characterization of electrocatalysts

Electrochemical hydrogenation reconstruction offered a potential strategy for converting precursor materials into highly active electrocatalysts[27,28]. Self-supported electrocatalysts prepared on conductive substrates could avoid the use of binders, thus exposing more active sites and improving catalytic activity. A self-supported hydrogen-rich titanium hydride electrocatalyst was prepared by cathodic in situ electrochemical hydrogenation reconstruction (Fig. 1a). To select the optimal hydrogenation potential, Cyclic Voltammograms (CV) tests were conducted for Ti FP within the range from 0 to − 1.3 V vs. RHE. As shown in Supplementary Fig. S1, the current density rose as the applied potential increased, indicating that the higher applied potential led to faster hydrogenation. To regulate the extent of electrochemical reduction, CV curves for activation covering different cycles (1^{st}, 10^{th}, 50^{th}, 100^{th}) within the range of 0 V to − 1.3 V vs. RHE were depicted in Fig. 1b. The corresponding polarization curves were displayed in Supplementary Fig. S2. The current density slightly increased between the 50^{th} and 100^{th} cycles, suggesting that the Ti FP could convert to $TiH_{1.97}$/Ti after activation for 50 cycles. Concurrently, the i-t curve at − 1.3 V vs. RHE for 1 h, shown in Fig. 1c, reached a maximum current density within 500 s and remained stable, implying that the electrochemical reconstruction of Ti FP to titanium hydride was a rapid process. In Fig. 1d, linear sweep voltammetry (LSV) of the sample at the initial stage and after hydrogenation for 500 s exhibited a significant difference in current density response. However, the current density response remained essentially unchanged after hydrogenation for 500 s and 3000 s, indicating that titanium hydride could be successfully prepared after hydrogenation for 500 s. Thus, a titanium hydride catalyst could be obtained quickly (hydrogenation for 500 s) through electrochemical hydrogenation reconstruction. As illustrated in Supplementary Fig. S3, the silver-gray Ti FP converted to black following a period of cathodic reconstruction. The load of titanium hydride catalyst on the electrode was determined to be 0.60 mg cm^{-2} by weighing the mass before and after reaction with 0.1 M HCl (Supplementary Fig. S4).

The X-ray diffraction (XRD) pattern demonstrated that the catalyst matched well with the standard cubic $TiH_{1.97}$ (PDF#07-0370) and hexagonal Ti (PDF#44-1294) (Fig. 1e), confirming that Ti and $TiH_{1.97}$ coexist in the catalyst. In addition, we also provided the standard cards for TiO_2 (PDF#73-2224), and TiH_2 (PDF#09-0371) (Supplementary Fig. S5a) and partially magnified the diffraction peaks at $TiH_{1.97}$ (200) (Supplementary Fig. S5b). By comparison, we found that there were no characteristic peaks of TiO_2 in the XRD pattern. Combining XAFS spectra (Fig. 2d) and XRD spectrum (Supplementary Fig. S5), it was clear that the characteristic peaks of $TiH_{1.97}$ were distinct from those of TiH_2, therefore, this catalyst had been confirmed as $TiH_{1.97}$. Besides, we scraped the black catalyst from the titanium fiber substrate and detected its phase structure through XRD. As shown in Supplementary Fig. S6, there are only three distinct characteristic peaks at 35.0°, 40.6°, and 58.8°, corresponding to the (111), (200) and (220) lattice planes of $TiH_{1.97}$. The scanning electron microscopy (SEM) images displayed that the obtained titanium hydride showed the nanosheet morphology and uniformly grew on titanium fiber (Fig. 1f, g and Supplementary Fig. S7). Furthermore, the titanium hydride nanosheets exhibited a smooth surface from the transmission electron microscopy (TEM) image (Fig. 1h), which was consistent with SEM results.

Chemical state and coordination environment of titanium hydride

The structural details of titanium hydride were confirmed by high-angle-annular-dark-field scanning transmission electron microscopy (HAADF-STEM). Figure 2a displays the high-resolution HAADF-STEM image of titanium hydride, where the marked d-spacings of 0.26 nm and 0.23 nm correspond to the (111) and (200) lattice planes of titanium hydride, respectively. The integrated pixel intensities revealed a periodic oscillation pattern, corresponding to the titanium hydride (111) and (200) planes (Fig. 2b). The selected area electron diffraction (SAED) pattern showed well-crystallized titanium hydride (Supplementary Fig. S8). As shown in Fig. 2c, the atomic-resolution HAADF-

https://doi.org/10.1038/s41467-024-53833-x

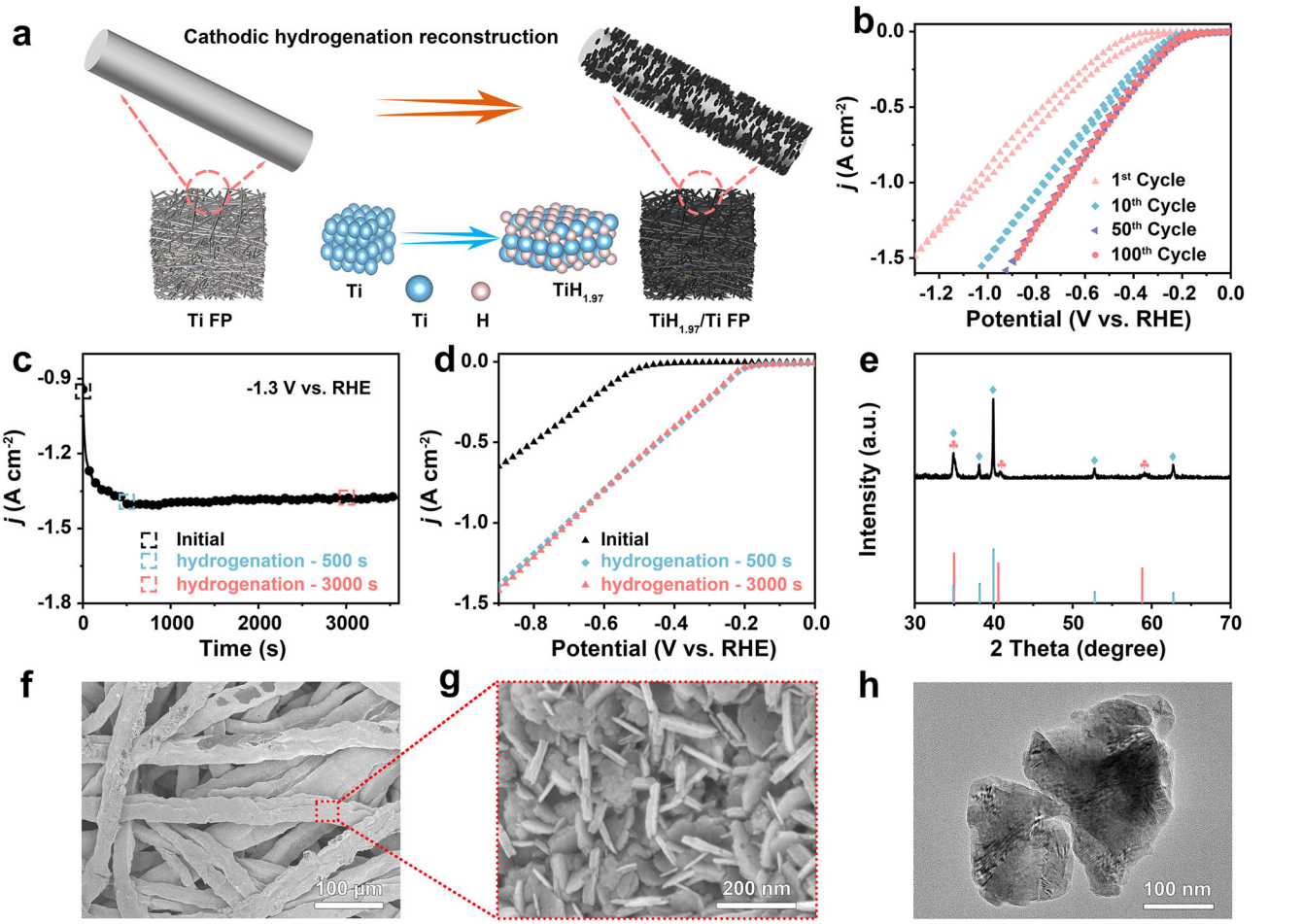

Fig. 1 | Preparation and characterization of electrocatalysts. a A schematic illustration of the electrochemical hydrogenation reconstruction of titanium fiber paper and their corresponding structure diagram. **b** CV curves of different cycles within the range from 0 to − 1.3 V vs. RHE (without iR compensation). **c** i-t curve at − 1.3 V vs. RHE (without iR compensation) for 1 h of Ti electrode. **d** LSV curves of Ti electrode before and after i-t testing (without iR compensation). **e** XRD spectrum. **f**, **g** SEM images (**h**) TEM image.

STEM image demonstrated the crystal structure of the titanium hydride (111) planes, with pink and blue circles representing hydrogen and titanium atoms, respectively. To examine the local coordination environment of Ti species in $TiH_{1.97}$, synchrotron-radiation-based X-ray absorption fine structure (XAFS) was utilized. The Ti K-edge XAFS spectra of $TiH_{1.97}$, the standard spectrum of Ti and TiH_2 were presented in Fig. 2d. Unlike Ti, TiH_2 showed no pre-edge peak, indicating the near-surface structure of TiH_2 transitioned from the hexagonal packed structure of Ti to a face-centered cubic structure[26]. $TiH_{1.97}$ showed a pre-edge peak similar to that of TiH_2, but the energy was lower than that of TiH_2, indicating that $TiH_{1.97}$ had the same face-centered cubic structure as TiH_2 (Supplementary Table S2). This difference also confirms that the sample we obtained was $TiH_{1.97}$ rather than TiH_2. In addition, the Ti foil exhibited a significant Ti-Ti scattering peak at 2.52 Å, which shifted to 2.72 Å in $TiH_{1.97}$ in the Fourier transformed (FT-EXAFS), suggesting an increase in the Ti-Ti bond length after hydrogen introduction (Fig. 2e). In addition, EXAFS curve-fit analysis was performed with Ti-Ti scattering paths, which was closely matched with $TiH_{1.97}$ (Fig. 2f, g). The wavelet transform (WT-EXAFS) analysis verified the distinction between the $TiH_{1.97}$ and Ti samples. The maximum intensity at the K (~ 7.36 $Å^{-1}$) and R + α (~ 2.72 Å) peak (Fig. 2h), attributed to the Ti-Ti bonds in the Ti WT contour plots of $TiH_{1.97}$, was higher than that of Ti (~ 6.69 $Å^{-1}$ and ~ 2.52 Å) (Fig. 2i), indicating that the introduction of hydrogen leads to an elongation of the Ti-Ti bond in $TiH_{1.97}$.

Electrocatalytic performance in NIRR

The NIRR performance of titanium hydride was evaluated using a H-type cell via electrochemical measurements. Linear sweep voltammetry (LSV) was performed to assess the activity and selectivity of the as-synthesized catalysts in 0.1 M KNO_3 and 1 M KOH (pH = 14), the current density of titanium hydride significantly increased after adding NO_3^- to the electrolyte (Fig. 3a), confirming that titanium hydride could effectively reduce NO_3^-. The corresponding current density of titanium hydride reached up to 1.05 A cm^{-2} at − 0.7 V vs. RHE, which was significantly superior to that of Ti FP (0.41 A cm^{-2}). At the same potential, the maximum FE of 99.11% with an NH_3 yield of 83.64 mg h^{-1} cm^{-2} was achieved (Fig. 3b and Supplementary Figs. S9, S10). In addition, the NIRR performance of titanium hydride was further evaluated using electrolytes with varying concentrations of NO_3^-. The NH_3 yields of NIRR for titanium hydride increased from 41.01 mg h^{-1} cm^{-2} to 96.05 mg h^{-1} cm^{-2} at − 0.7 V vs. RHE across a range of NO_3^- concentrations from 0.02 M to 1.00 M (Fig. 3c and Supplementary Fig. S11), indicating its potential in treating water sources with varying levels of NO_3^- pollution. In addition, as the nitrate concentration increased from 0.02 M to 0.06 M, the FE gradually increased from 73.30 % to 99.21 %. When the concentration continued to increase from 0.07 M to 1.00 M, FE showed a slight downward trend from 99.18 % to 93.34 %. This phenomenon was mainly attributed to the competitive reaction with HER at low concentrations and the influence of the tandem reaction of hydrogenation at high concentrations. At low NO_3^-

https://doi.org/10.1038/s41467-024-53833-x

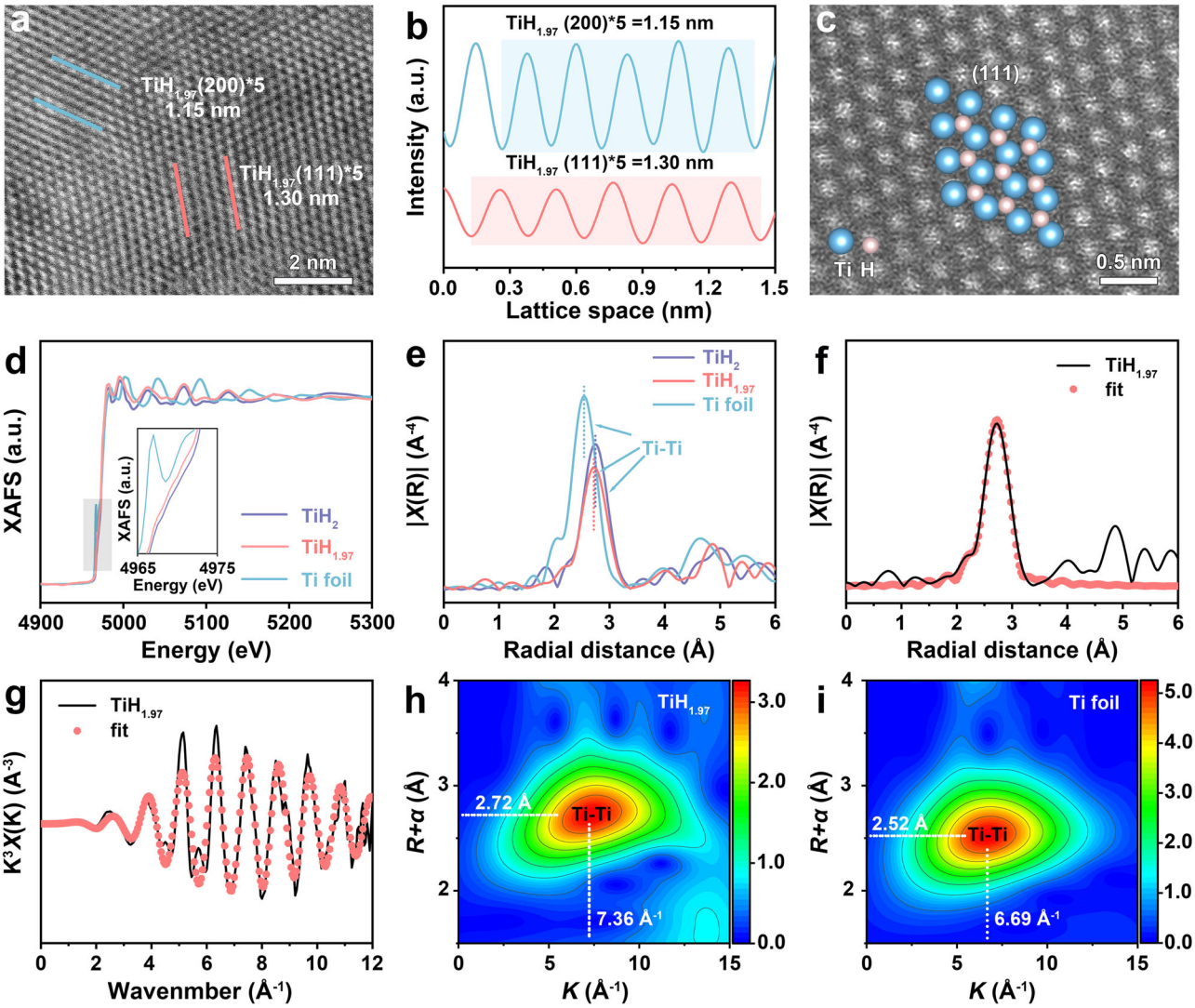

Fig. 2 | Chemical state and coordination environment of titanium hydride. **a** High-resolution HAADF-STEM image of titanium hydride. **b** Integrated pixel intensities in the selected regions of (**a**). **c** Atomic-resolution HAADF-STEM image of titanium hydride. **d** XAFS spectra and (**e**) FT-EXAFS spectra at Ti K-edge. **f** Ti K-edge EXAFS (line) and curve fit (points) for $TiH_{1.97}$ in R-space. **g** The fit curve of k3χ(k) oscillation functions in k-space for $TiH_{1.97}$. **h**, **i** WT-EXAFS of Ti for $TiH_{1.97}$ and Ti foil.

concentrations, the competitive reactions between NIRR and hydrogen evolution reaction (HER) played a dominant role. At high NO_3^- concentrations, the tandem catalytic reaction between nitrate activation and hydrogenation played a dominant role. Their relationship diagram is shown in Supplementary Fig. S12., Since stability was a crucial factor for industrial applications, a stability test was performed at − 0.7 V vs. RHE, with periodic updates taken every 3 h (Fig. 3d). In each stage, the yield and FE remained stable for the first two hours, but the NIRR performance showed a marked decline in the final hour, which was correlated with the reduction in NO_3^- concentration. It was evident that the decline in NIRR performance could be recovered by renewing the electrolyte, highlighting the high robustness of titanium hydride in NIRR applications. After long-time cyclic testing, we had thoroughly characterized the titanium hydride catalyst. The SEM and XRD analyses of the titanium hydride showed that the morphology and phase of the material had not changed (Supplementary Figs. S13, S14). The above results further confirmed the stability of titanium hydride during the NIRR process. We also tested the XRD spectrum of the electrode during NIRR at applied potentials of − 0.1, − 0.2, − 0.4, − 0.6, − 0.8, and − 1.0 V vs. RHE. Based on ex-situ XRD patterns (Supplementary Fig. S15a) and local magnification of the (200) and (220) characteristic peaks (Supplementary Fig. S15b, c), the phase of titanium hydride did not change during the NIRR process, implying that the Ti to H ratio in the active material remained unchanged. This result also confirmed our proposed viewpoint: In titanium hydride, the lattice hydrogen spills out and participates in the hydrogenation reaction during the nitrate reduction process, while the H generated by water electrolysis replenishes the hydrogen consumption in titanium hydride.

To assess the wastewater treatment potential and ammonia production efficiency of titanium hydride. As illustrated in Fig. 3e, the NO_3^- concentration gradually decreased during NIRR at − 0.7 V vs. RHE. After 3 h of electrocatalysis, only 5.08 ppm of NO_3^--N and 0.89 ppm of NO_2^--N were left, both well below the WHO standards for drinking water, indicating a NO_3^- conversion rate of 98.50 % and an NH_3 selectivity of 98.20 %. The 0.25 cm^2 catalyst was shown to effectively reduce NO_3^- and NO_2^- levels in 50 mL of simulated industrial wastewater to meet drinking water standards within 3 h, showcasing its notable wastewater treatment capacity. Under the same conditions (1 M KOH + 0.1 M NO_3^-), the titanium hydride catalyst demonstrated a significantly higher NH_3 yield rate (83.64 mg h^{-1} cm^{-2}) and FE (99.11 %) at the potential of − 0.7 V vs. RHE compared to the latest NIRR

https://doi.org/10.1038/s41467-024-53833-x

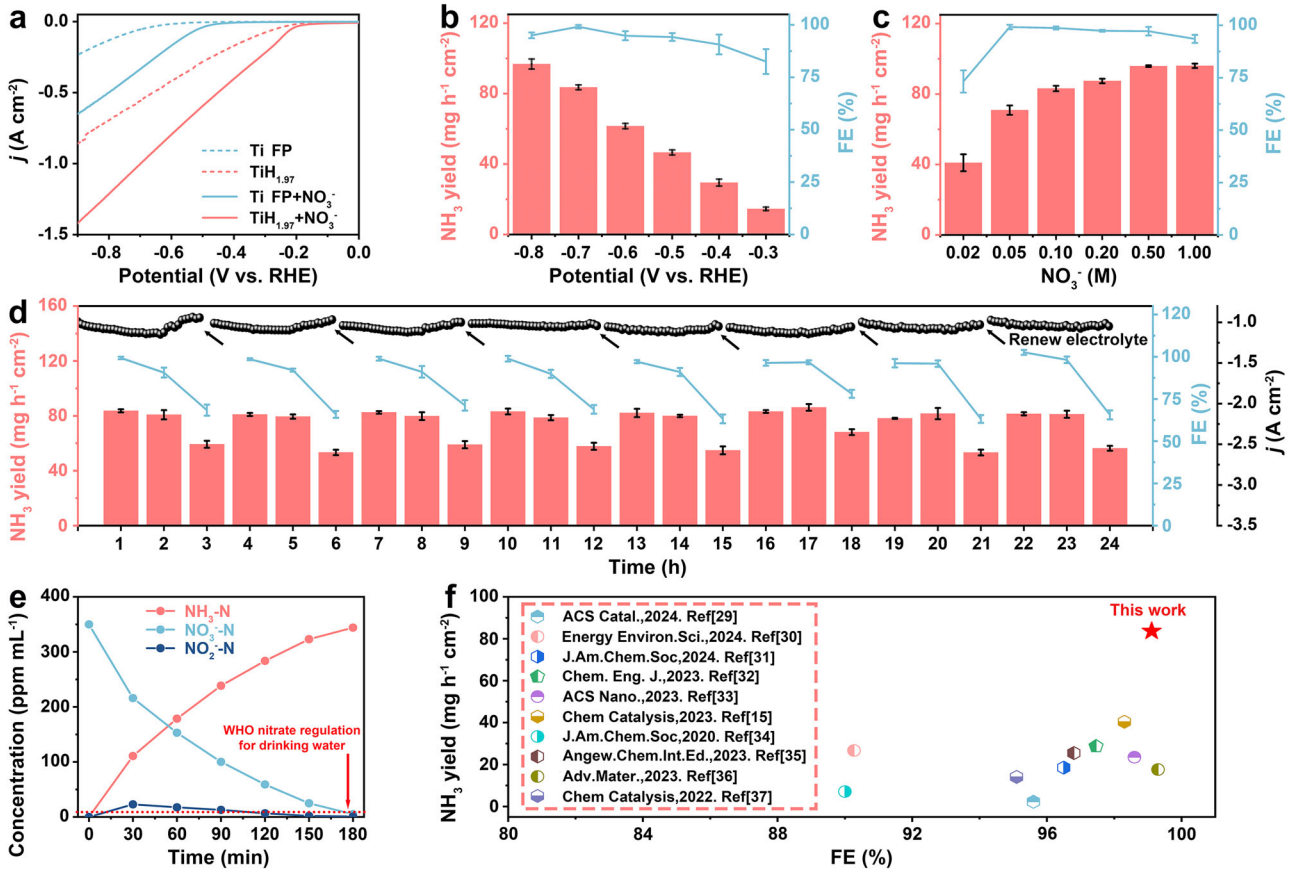

Fig. 3 | Electrocatalytic performance in NIRR. a LSV curves of Ti FP and titanium hydride with and without NO_3^- (without iR compensation). **b** NH_3 yields and FEs for titanium hydride against various work potentials in 1 M KOH solution with 0.1 M NO_3^- (without iR compensation). **c** NH_3 yields and FEs for titanium hydride at different concentrations of NO_3^- (without iR compensation). **d** Stability test at − 0.7 V vs. RHE (without iR compensation) with periodic updates taken every 3 h. **e** The time-dependent concentration change of NO_3^--N, NO_2^--N and NH_3-N (without iR compensation). **f** Comparison of the NIRR performance of the titanium hydride with the reported electrocatalyst (The nitrate concentrations of these reports were equal to 0.1 M). The NH_3 yields and FEs are calculated once per hour. Error bars indicate there lative standard deviations of the mean ($n = 3$).

electrocatalysts documented in the literatures[15,29–37], and the ECSA-normalized NH_3 yield up to 0.72 while maintaining NIRR performance that was on par with or superior to that of its competitors (Fig. 3f, Supplementary Fig. S16 and Supplementary Table S3). In addition, the voltage ranges used in various literatures were different, and we also compared the NIRR performance under the same NO_3^- concentration with different voltages, our catalyst could achieve high FE and NH_3 yield rate at high voltages as shown in Supplementary Fig. S17, which was very important in ammonia synthesis, and this performance was difficult to achieve in other catalysts. We also calculated the NIRR performance based on the mass of the titanium hydride catalyst loaded on the electrodes. As could be seen from Supplementary Fig. S18 and Supplementary Table S4, under the same test conditions (1 M KOH + 0.1 M NO_3^-), titanium hydride catalyst still had a significant advantage in terms of NH_3 yield (139.33 mg h^{-1} mg $_{cat}^{-1}$ at − 0.7 V vs. RHE).

Proposed lattice hydrogen transfer mechanism

To reveal the reaction mechanism for enhancing NIRR catalytic activity, isotope tracking experiments were used to investigate the electrochemical behavior of lattice hydrogen transferred from titanium hydride. The model diagram for the positive and reverse verification of isotope-labeled lattice hydrogen transfer during the NIRR process is shown in Fig. 4a. For the positive verification, titanium and titanium hydride serving as electrocatalysts and using 1 M NaOD + 0.1 M KNO_3 in D_2O solution as the electrolyte for NIRR, the peaks at 7.05, 7.14 and 7.23 ppm in the ^1H NMR spectrum of Ti were identified as the characteristic peaks of ND_4^+. In the ^1H NMR spectrum of titanium hydride, besides the characteristic peaks of ND_4^+, a set of typical peaks for NH_4^+ at 7.03, 7.12, and 7.20 ppm was observed, which were attributed to the lattice hydrogen in titanium hydride (Fig. 4b). After the isotope tracking experiments test, we conducted XRD spectrum on the electrodes. As shown in Supplementary Fig. S19, compared to titanium hydride before isotope experiments, the (111) crystal plane of the sample exhibited a double peak and a slight shift, which was due to the introduction of deuterium (D). Apart from that, the other diffraction peaks were the same as the characteristic peaks of titanium hydride, indicating that the molecular formula of titanium hydride did not change, except that D replaced the H element in the lattice. This result further verified that lattice hydrogen was involved in the hydrogenation reaction of NIRR, and the hydrogen in water was replenished to lattice hydrogen of titanium hydride. This dynamic balance of H* consumption and replenishment improved the efficiency of NIRR. In the reverse verification, using the same method, we synthesized the titanium deuteride catalyst (The XRD and solid-state NMR spectra used to confirm the successful synthesis of titanium deuteride were shown in Supplementary Fig. S20) and used 1 M NaOH + 0.1 M KNO_3 in H_2O solution as the electrolyte for NIRR. In the ^1H NMR spectrum of titanium deuteride, in addition to the characteristic peaks of NH_4^+, the typical peaks of ND_4^+ were also noted, indicating their origin from

https://doi.org/10.1038/s41467-024-53833-x

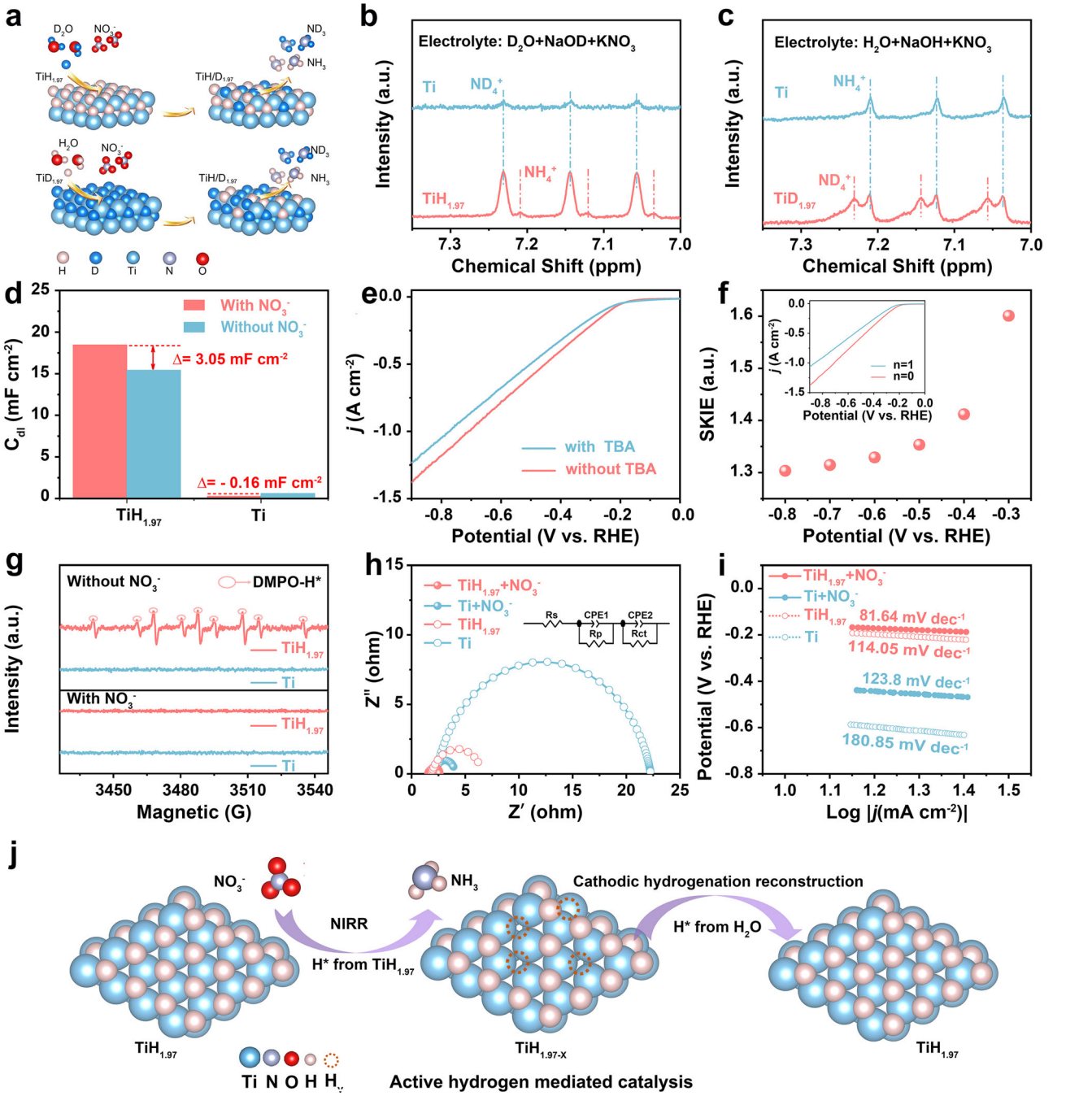

Fig. 4 | Proposed lattice hydrogen transfer mechanism. a Model diagrams for positive and reverse validation of isotope-labeled lattice hydrogen transfer in the NIRR process. **b** Isotope labeled lattice hydrogen transfer in NIRR process for $TiH_{1.97}$ (positive validation) and (**c**) $TiD_{1.97}$ (reverse validation). **d** the double layer capacitance in the electrolyte with and without NO_3^- at a potential range without Faraday reaction. **e** LSV curves of titanium hydride with or without TBA (without iR compensation). **f** SKIE values under different applied potentials. Inset of Fig. 4f were LSV curves of titanium hydride in different proportions of mixed D_2O and H_2O solution, $n = D_2O/ [D_2O + H_2O]$ (without iR compensation). **g** DMPO-involved ESR spectra of the titanium hydride and Ti FP under different electrolysis conditions. **h** The Nyquist plots (without iR compensation) and (**i**) The Tafel slope (without iR compensation). **j** Schematic of the reaction mechanism.

lattice deuterium in titanium deuteride (Fig. 4c). Through the aforementioned positive and reverse verification, we had concluded that the lattice hydrogen in titanium hydride indeed participated in the hydrogenation reaction of NIRR. Lattice hydrogen effused from titanium hydride and was converted into H*, while the H in the solution ensured the formation of titanium hydride. The reversible equilibrium reaction between lattice hydrogen and H* not only enhanced the electrocatalytic activity of NIRR but also exhibited notable catalytic stability. In addition, the isotopic labeling experiments using $^{15}NO_3^-$ and $^{14}NO_3^-$ as reactants were conducted to confirm the nitrogen in NH_3 originated from NO_3^-, which were shown in Supplementary Fig. S21.

As shown in Fig. 4d and Supplementary Figs. S22, S23, the CV curves of Ti FP titanium hydride were tested at a potential range without Faraday reaction (0.12 V ~ 0.22 V vs. RHE), respectively. Titanium hydride exhibited a larger double-layer capacitance (C_{dl}) in NO_3^- solution (18.47 mF cm^{-2}) than that in the solution without NO_3^- (15.42 mF cm^{-2}), demonstrating that its surface contained a greater

number of active sites. For NIRR at the solid-liquid interface, which was also much superior to that of Ti FP (0.45 mF cm^{-2} with NO_3^- solution and 0.61 mF cm^{-2} without NO_3^- solution), verifying the facilitated NO_3^- coverage and adsorption. Tert-butanol (TBA) was used as a specific radical quenching reagent to evaluate the role of H* in NIRR[4]. As could be seen from Fig. 4e, the addition of 1 ml of TBA to the electrolyte significantly reduces the current density in LSV, indicating that the H* was quenched, leading to the decay in performance of NIRR. To study the role of protons in NIRR, the solvent kinetic isotope effect (SKIE) was assessed by comparing the current density in a pure protic electrolyte ($KOH + H_2O + KNO_3$) to that in a pure deuterium electrolyte ($NaOD + D_2O + NaNO_3$). The inset of Fig. 4f showed that an increase in the proportion of deuterium led to a decrease in current density and the observed SKIE values were all greater than 1 at various applied potentials (Fig. 4f). These results suggested that protons enhanced the catalytic activity of NO_3^- reduction to NH_3[6]. The Electron Spin Resonance (ESR) spectra were detected using 5,5-dimethyl-1-pyrroline-N-oxide (DMPO) as the H* trapping reagent to verify whether H* could participate in the hydrogenation reaction in NIRR[17,35]. As illustrated in Fig. 4g, the typical strong peak with intensity ratios of 1: 1: 2: 1: 2: 1: 2: 1: 1[38] was observed for titanium hydride in 1 M KOH solution without NO_3^-, which was attributed to H*. However, no H* was detected for Ti FP under the same testing conditions, indicating that the lattice hydrogen in titanium hydride could overflow and form H*. Meanwhile, the signal intensity of DMPO-H nearly disappeared when 0.1 M NO_3^- was added to the cathode electrolyte, confirming that the H* was consumed by NO_3^- during the NIRR process. This result aligned with the findings in Fig. 4b, c, which highlighted the reversible equilibrium reaction between lattice hydrogen and activate hydrogen (H*). The kinetics of charge transfer in the catalyst electrodes were evaluated using Nyquist plots under open circuit conditions (Fig. 4h). These plots were meticulously fitted with an equivalent circuit diagram. The resistances corresponding to substrate diffusion, potential loss, and charge transfer at the electrode/electrolyte interface were labeled as R_s, R_p, and R_{ct}, respectively. The fitted data is shown in Supplementary Table S1. The constant phase element (CPE) value for titanium hydride was higher than that for Ti, indicating a higher efficiency in active species adsorption for titanium hydride[39,40]. The R_{ct} of titanium hydride was significantly lower than that of Ti FP in a 1 M KOH solution with 0.1 M NO_3^-. The R_{ct} of titanium hydride in 1 M KOH solution with 0.1 M NO_3^- was significantly smaller than in 1 M KOH, corresponding to faster NIRR kinetics at the titanium hydride electrode-electrolyte interface. Electrokinetic analysis was further detected to determine the rate-determining step (RDS) of NIRR for the titanium hydride and Ti FP catalysts (Fig. 4i). The Tafel slope of titanium hydride was 81.64 mV dec^{-1}, much inferior to 120 mV dec^{-1}, indicating that the RDS for NIRR of titanium hydride was the first one-electron transfer occurring during the NO_3^- to NO_2^- conversion[41]. The higher Tafel slope of Ti FP (123.8 mV dec^{-1}) indicated that the NIRR over Ti FP was restricted by the initial adsorption and activation of NO_3^- [42]. As the Tafel slope value (81.64 mV dec^{-1}) of titanium hydride in 1 M KOH solution with 0.1 M NO_3^- was much smaller than that of titanium hydride (114.05 mV dec^{-1}) in 1 M KOH, it revealed that NIRR was more conducive to occurrence compared with competing reactions of HER[41,43]. According to the results mentioned above, a possible enhanced NIRR mechanism of titanium hydride was proposed, as illustrated in Fig. 4j. On the one hand, H* from titanium hydride participated in the hydrogenation of NO_3^- to synthesize NH_3. On the other hand, the electrochemical hydrogenation reconstruction reaction occurred simultaneously with NIRR, which converted the $TiH_{1.97-x}$ into $TiH_{1.97}$. The above reversible equilibrium reaction between H* transfer and hydrogenation reconstruction not only improved the electrocatalytic activity of NIRR but also exhibited notable catalytic stability.

With the aim of confirming the generality of lattice hydrogen transfer from catalyst to improve NIRR, the same method was also used to electrochemically hydrogenate and reconstruct different metal foils, including Pd, Ta, and V. The electrochemical measurements, morphology (SEM), and phase (XRD) of palladium hydride (Supplementary Fig. S25), tantalum hydride (Supplementary Fig. S26), and vanadium hydride (Supplementary Fig. S27) were comprehensively researched. The hydrogenation reconstruction of the samples significantly improved the NIRR performance. These results demonstrated that lattice hydrogen transfer from the catalyst was a generalized route to elevate NIRR performance. In addition, this mechanism of lattice hydrogen facilitating catalytic reactions might also have implications for other hydrogenation reactions, such as the hydrogenation of CO_2.

Theoretical calculation analysis

Density Functional Theory (DFT) calculations have revealed the competitive behavior between different sources of H* during the hydrogenation process of NIRR (one was from the electrolyte, the other was from the lattice hydrogen in titanium hydride). According to the experimental results of XRD and HAADF-STEM, $TiH_{1.97}$ (111) and Ti (101) slab models were constructed (more calculation details could be found in supporting information). At first, the adsorption free energy of *H (ΔG_{*H}) on titanium and titanium hydride was calculated (Fig. 5a) a relatively lower value of ΔG_{*H} (− 1.20 eV) means a stronger adsorption of Ti for *H. On the contrary, the capture of *H by titanium hydride was quite difficult due to a higher ΔG_{*H} of 0.63 eV, which also suggested that the hydrogenation of nitrate on titanium hydride was probably the least appealing option. However, once an H vacancy was formed, titanium hydride could exhibit extremely strong *H capture ability ($\Delta G_{*H} = -1.64eV$). This result indicated that when lattice hydrogen overflows in titanium hydride to form an H vacancy ($TiH_{1.97}$-H_v), it exhibited a relatively strong ability to adsorb H*. Meanwhile, the calculated results of ΔG_{*H} on Ti and $TiH_{1.97}$-H_v also indicated the feasible thermodynamically from Ti to $TiH_{1.97}$. Figure 5b illustrates the competitive dynamics between the adsorption of H* from different sources during the initial protonation stage of NIRR. The calculated reaction energy barriers for the transformation of $*NO_3$ to $*NO_3H$ using H* derived from H_2O and lattice hydrogen were 0.68 eV and 0.31 eV, respectively (the theoretical models of initial state, transition state, and final state were shown in Supplementary Fig. S28). This data indicated that H* produced by lattice hydrogen was preferentially utilized in NIRR. As a result, we could conclude that lattice hydrogen would preferentially participate in the NIRR rather than the H* from the H_2O solution. It was worth mentioning that the adsorption of nitrate could weaken the surface Ti-H bond due to the obvious charge loss behavior of surface H atoms (Supplementary Fig. S29), which was beneficial for the further reaction between nitrate and lattice hydrogen.

To further clarify the reaction mechanism of NIRR, Fig. 5c illustrates the reaction-free energy of each elementary step on titanium hydride and titanium. The adsorption configurations of reaction intermediates are shown in Supplementary Fig. S30. It could be found that the first protonation step (from $*NO_3$ to $*NO_3H$) was the most thermodynamically uphill elementary step (PDS), which was also known as the potential determining step, for both titanium hydride and titanium. By checking the reaction free energy of PDS, one could see that $TiH_{1.97}$ could exhibit an extremely high catalytic activity for NIRR owing to the optimal limiting potential of 0.12 V. As a comparison, the limiting potential of NIRR on Ti was as high as 0.99 V, implying a lower catalytic activity. More importantly, to understand the facilitating role of lattice hydrogen transfer in NIRR, we analyzed the adsorption strengths of key intermediates $*NO_3$, $*NO_3H$, and $*NO_2$ on titanium hydride (Fig. 5d). When lattice hydrogen participates in the formation of NO_3H, an H vacancy was generated on titanium hydride, which significantly enhanced the adsorption strength of $TiH_{1.97}$ to NO_3H. As a result, the adsorption strength of $*NO_3H$ ($\Delta G = -1.96eV$)

https://doi.org/10.1038/s41467-024-53833-x

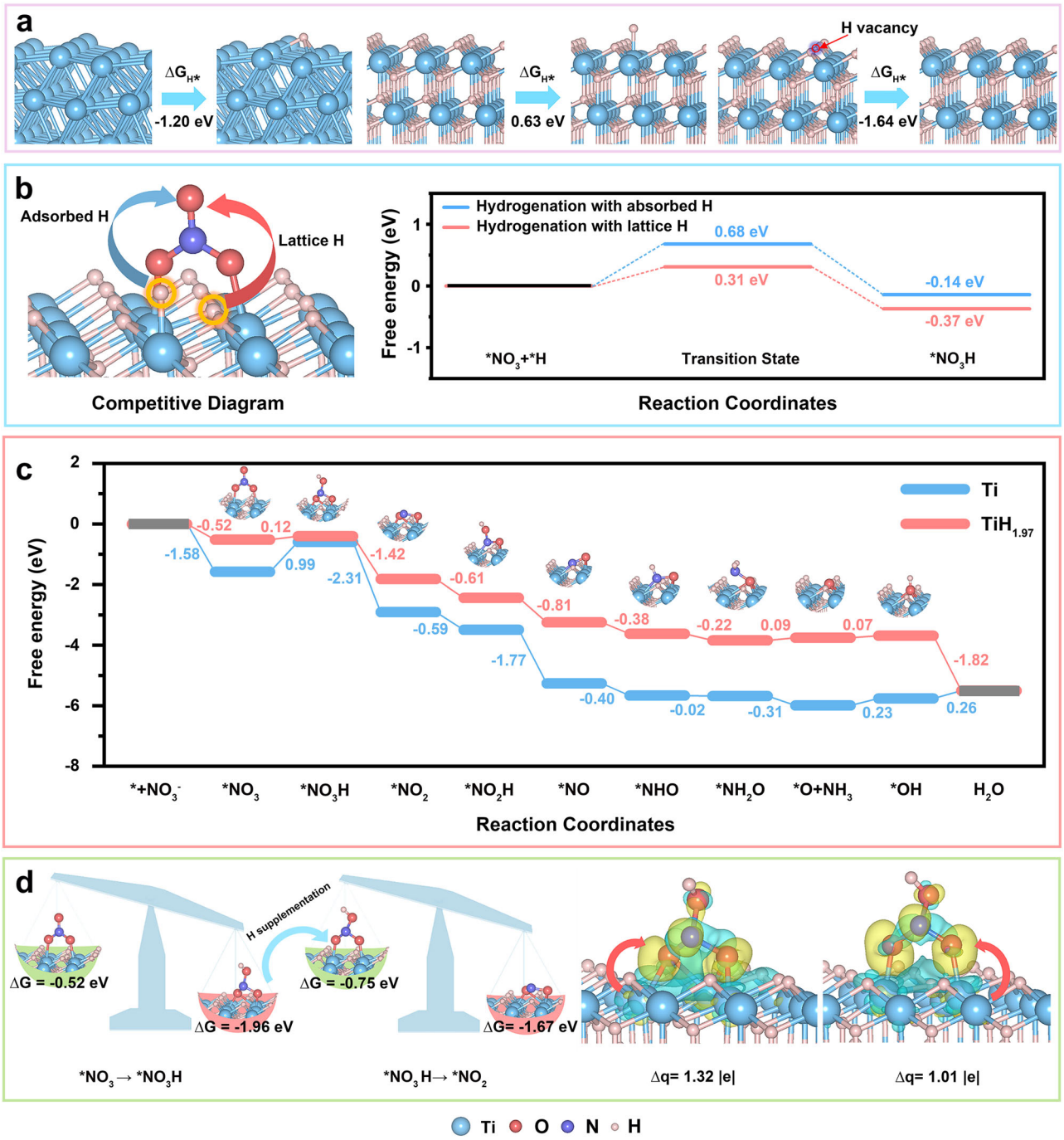

Fig. 5 | Theoretical calculation analysis. a Calculated adsorption free energy of H* (ΔG_{H^*}) on Ti, $TiH_{1.97}$, and $TiH_{1.97}$ with H vacancy. **b** Reaction energy barriers of nitrate hydrogenation through different sources of H (including adsorbed H and lattice H). **c** Reaction free energy of NIRR on Ti (blue curve) and $TiH_{1.97}$ (pink curve). **d** Schematic diagram for balancing adsorption strength of key intermediate through the dynamic regulation of lattice H.

was much stronger than that of $*NO_3$ ($\Delta G = -0.52eV$), suggesting a lower thermodynamic potential barrier from $*NO_3$ to $*NO_3H$. Interestingly, when this H defect was restored (this process was highly thermodynamically prone to occur according to the calculation results of Fig. 5a), the adsorption strength of $*NO_3H$ was greatly weakened ($\Delta G = -0.75e$), which provided favorable conditions for the next reaction. Calculated charge density difference (Fig. 5d) further revealed that the reversible equilibrium reaction between lattice hydrogen and activated hydrogen (H*) could effectively tune the charge transfer behavior from titanium hydride to adsorbate, thus balancing the adsorption strength of key intermediate.

Discussion

In summary, the titanium hydride electrocatalyst synthesized by electrochemical hydrogenation reconstruction of titanium fiber paper achieved an ampere-level current density of 1.05 A cm^{-2} for NIRR with a high NH_3 yield rate of 83.64 mg h^{-1} cm^{-2} and a FE of 99.11% at − 0.7 V vs. RHE. Through electrochemical evaluation and theoretical calculation analysis, the lattice hydrogen transfer mechanism was proposed and confirmed that the reversible equilibrium reaction between lattice hydrogen and activate hydrogen (H*) not only improved the electrocatalytic activity of NIRR but also demonstrated notable catalytic stability. We believed that the perspective centered

on lattice hydrogen transfer would expand the possibilities for designing metal hydrides as electrocatalysts and introduce a universal strategy for efficient NIRR.

Methods

Chemicals and materials

Ti fiber paper (Ti FP, 99.9%) was purchased from Suzhou Sinero Technology Co., Ltd. Potassium hydroxide (KOH, 85%), sodium hypochlorite (NaClO, available chlorine 5.2% of aqueous solution), hydrochloric acid (HCl, 12 mol L^{-1}), sulfamic acid (H_3NO_3S, 96%), salicylic acid ($C_7H_6O_3$, 99.5%), Sodium hydroxide (NaOH, ≥ 96.0%) and potassium nitrate (KNO_3, 99.0%) were obtained from Sinopharm Chemical Reagent Co., Ltd. Potassium sodium tartrate tetrahydrate ($C_4H_4O_6KNa{\cdot}4H_2O$,≥ 99.0%) and sodium nitroferricyanide dihydrate ($C_5FeN_6Na_2O{\cdot}2H_2O$, 99%) were supplied with Shanghai Macklin Biochemical Co., Ltd. Sodium nitrate-^{15}N ($K^{15}NO_3$, 99.0 atom% ^{15}N) and dimethyl sulfoxide-d_6 (DMSO-d_6, 99.9 atom% D) were purchased from Shanghai Aladdin Biochemical Technology Co., Ltd. Deuterium water (D_2O, 99.8%), Sodium deuteroxide (NaOD, 99.5 atom% D, 40% in D_2O) and sulfuric acid-d_2 solution (D_2SO_4, 99 atom% D, 96–98% in D_2O) were purchased from Anhui Zesheng Technology Co., Ltd. Deionized water was obtained from the Barnstead Ultrapure Water System (Smart2Pure, 18.2 MΩ cm). Unless noted otherwise, all reagents were used without further purification.

Synthesis of titanium hydride

CHI 760E electrochemical workstation (Chenhua, Shanghai) was used to synthesize titanium hydride. Ti FP (thickness: 0.05 mm, size: 0.5 × 0.5 cm^2) was sonicated utilizing HCl solution (15 ml, 10 min) and then in water (15 ml, 5 min) and ethanol (15 ml, 5 min), followed by drying in air. The electrochemical hydrogenation reconstruction was conducted using a standard three-electrode configuration H-type electrochemical cell (Supplementary Fig. S33) containing Ti FP as the working electrode (WE), a platinum plate as the counter electrode (CE), and a Hg/HgO as the reference electrode (RE). The electrolyte was composed of 60 mmol KOH and 6 mmol KNO_3 dissolved into 60 mL deionized water. The constant potential electrochemical hydrogenation reconstruction was then carried out at −1.3 V (vs. RHE) at 25 °C. The hydrogenation reconstruction time of titanium hydride was 3600 s. The electrode was thoroughly rinsed three times with deionized water. After hydrogenation reconstruction, the titanium hydride was carefully displaced from the electrolyte and rinsed three times with ethanol and water, the titanium hydride following dried by Ar flow. The H-type electrolytic cell for conducting NIRR operated in an alkaline environment and used a Nafion membrane for separation to prevent the dissolution of the Pt electrode and its subsequent deposition on the electrocatalyst. The element mapping results overlapped with Supplementary Fig. S7, showed that only the distribution of Ti elements was present in the sample, with no Pt atoms. This indicated that the Pt electrode had not been deposited on the catalyst.

Preparation of the electrolyte

To prepare the 1 M KOH electrolyte solution (pH = 13.87 ± 0.16), 1 mol KOH was weighed and added to a 1 L beaker containing deionized water (Supplementary Fig. S34). The mixture was stirred until dissolved and cooled to room temperature, then transferred to a 1 L volumetric flask, made up to the mark. The mark and stored at room temperature. The 1 M KOH with 0.1 M KNO_3 electrolyte solution (pH = 13.92 ± 0.12) was prepared by weighing 2 mol of solid KOH and adding it to a beaker with deionized water. After stirring to dissolve and cooling to room temperature, 0.2 mol of solid KNO_3 was added to the 1 L beaker and mixed evenly before being stored at room temperature in a 2 L volumetric flask.

Electrochemical measurements

The electrochemical measurements were conducted with an electrochemical workstation (Chenhua, 760E) using an H-type electrochemical cell that was divided by a Nafion 211 membrane. The $TiH_{1.97}$/Ti acted as the WE, while the RE was a Hg/HgO, and a platinum foil was used as the CE. All potentials were referenced to the RHE scale using the following equation:

$$E\,(V\,vs.RHE) = E\,(V\,vs.Hg/HgO) + 0.0591 \times pH + 0.098$$

Prior to the NIRR test, LSV was conducted until the polarization curves stabilized, with a sweep rate of 10 mV s^{-1} from 0 to − 0.9 V vs. RHE. Constant potential tests were performed across various applied potentials in a standard H-type cell containing 50 mL of electrolyte, stirred at 600 rpm for 1 hour at 25 °C. The error bars indicated the relative standard deviations based on a minimum of three repeated measurements. EIS was performed across spanning a frequency range of 0.1 Hz to 10^5 Hz. All electrochemical data were presented without iR compensation, and the solution resistance (R_s) was also noted (Supplementary Fig. S35). CV was performed with the non-Faradaic region at various scan rates from 40 to 200 mV s^{-1} to evaluate the C_{dl}, which could be used to calculate the ECSA using the equation:

$$ECSA = C_{dl}/C_s \times A$$

where C_{dl} was the catalyst's double-layer capacitance, Cs was the capacitance of an anatomically smooth planar surface (40 μF cm^{-2} in alkaline media), and A was the electrode area[44,45].

Calculation of the yield, conversion rate, selectivity, and Faradaic efficiency

For NIRR, the NH_3 yield was assessed through the equation:

$$Yield_{NH_3} = (C_{NH_3} \times V)/(M_{NH_3} \times t \times S) \quad (1)$$

The FE was calculated using the electric charge used for the ammonia product relative to the total charge passed through the electrode, as described by the equation.:

$$FE = (8F \times C_{NH_3} \times V)/(M_{NH_3} \times Q) \quad (2)$$

where C_{NH3} specified the concentration of NH_3 in aqueous solution, V signified the volume of cathode electrolyte, M_{NH3} denoted the molar mass of NH_3, t represented the reduction reaction time (h), S specified the geometric area of catalyst (cm^2), F specified the Faradaic constant (96485 C mol^{-1}), Q denoted the total electric charge passing the catalytic electrode.

Data availability

The authors declare that the data supporting the findings of this study are available within this article and its Supplementary Information file, or from the corresponding authors upon request. Source data are provided in this paper.

References

1. Fan, K. et al. Active hydrogen boosts electrochemical nitrate reduction to ammonia. *Nat. Commun.* **13**, 7958 (2022).
2. Guo, J. et al. Mass transport modifies the interfacial electrolyte to influence electrochemical nitrate reduction. *ACS Sustain. Chem. Eng.* **11**, 7882–7893 (2023).
3. Kim, K.-H. et al. Energy-efficient electrochemical ammonia production from dilute nitrate solution. *Energy Environ. Sci.* **16**, 663–672 (2023).
4. Wang, Y., Li, H., Zhou, W., Zhang, X., Zhang, B. & Yu, Y. Structurally disordered RuO_2 nanosheets with rich oxygen vacancies for

enhanced nitrate electroreduction to ammonia. *Angew. Chem. Int. Ed.* **61**, e202202604 (2022).
5. Jiang, H. et al. Enabled efficient ammonia synthesis and energy supply in a zinc-nitrate battery system by separating nitrate reduction process into two stages. *Angew. Chem. Int. Ed.* **62**, e202218717 (2023).
6. Zhou, J. et al. Regulating active hydrogen adsorbed on grain boundary defects of nano-nickel for boosting ammonia electrosynthesis from nitrate. *Energy Environ. Sci.* **16**, 2611–2620 (2023).
7. Sun, L. & Liu, B. Mesoporous PdN alloy nanocubes for efficient electrochemical nitrate reduction to ammonia. *Adv. Mater.* **35**, e2207305 (2023).
8. Du, L., Xing, L., Zhang, G., Liu, X., Rawach, D. & Sun, S. Engineering of electrocatalyst/electrolyte interface for ambient ammonia synthesis. *SusMat* **1**, 150–173 (2021).
9. Wang, Y., Xu, Y., Cheng, C., Zhang, B., Zhang, B. & Yu, Y. Phase-regulated active hydrogen behavior on molybdenum disulfide for electrochemical nitrate-to-ammonia conversion. *Angew. Chem. Int. Ed.* **63**, e202315109 (2024).
10. Zhang, M., Ai, X., Liang, X., Chen, H. & Zou, X. Key role of local chemistry in lattice nitrogen-participated N_2-to-NH_3 electrocatalytic cycle over nitrides. *Adv. Funct. Mater.* **33**, 2306358 (2023).
11. Shen, P., Wang, G., Chen, K., Kang, J., Ma, D. & Chu, K. Selenium-vacancy-rich WSe_2 for nitrate electroreduction to ammonia. *J. Colloid Interface Sci.* **629**, 563–570 (2023).
12. Li, Y. et al. Green and large-scale production of ammonia: Laser-driven pyrolysis of nitrogen-enriched biomass. *SusMat* **3**, 533–542 (2023).
13. Xu, Z. et al. Continuous ammonia electrosynthesis using physically interlocked bipolar membrane at 1000 mA cm^{-2}. *Nat. Commun.* **14**, 1619 (2023).
14. Gu, Z., Zhang, Y., Wei, X., Duan, Z., Gong, Q. & Luo, K. Intermediates regulation via electron-deficient Cu sites for selective nitrate-to-ammonia electroreduction. *Adv. Mater.* **35**, 2303107 (2023).
15. Li, J., Li, H., Fan, K., Lee, J. Y., Xie, W. & Shao, M. Electrocatalytic nitrate reduction to ammonia coupled with organic oxidation. *Chem. Catal.* **3**, 100638 (2023).
16. Liu, M. J., Miller, D. M. & Tarpeh, W. A. Reactive separation of ammonia from wastewater nitrate via molecular electrocatalysis. *Environ. Sci. Technol. Lett.* **10**, 458–463 (2023).
17. Yu, W. et al. Laser-controlled tandem catalytic sites of CuNi alloys with ampere-level electrocatalytic nitrate-to-ammonia reduction activities for Zn–nitrate batteries. *Energy Environ. Sci.* **16**, 2991–3001 (2023).
18. Zhao, T. et al. Homonuclear dual-atom catalysts embedded on N-doped graphene for highly efficient nitrate reduction to ammonia: From theoretical prediction to experimental validation. *Appl. Catal. B Environ.* **339**, 123156 (2023).
19. Wang, Y., Wang, C., Li, M., Yu, Y. & Zhang, B. Nitrate electroreduction: mechanism insight, in situ characterization, performance evaluation, and challenges. *Chem. Soc. Rev.* **50**, 6720–6733 (2021).
20. Zhang, S. et al. Fe/Cu diatomic catalysts for electrochemical nitrate reduction to ammonia. *Nat. Commun.* **14**, 3634 (2023).
21. Fernández, J. F., Cuevas, F. & Sánchez, C. Simultaneous differential scanning calorimetry and thermal desorption spectroscopy measurements for the study of the decomposition of metal hydrides. *J. Alloy. Compd.* **298**, 244–253 (2000).
22. Kumar, P., Singh, S., Hashmi, S. A. R. & Kim, K.-H. MXenes: Emerging 2D materials for hydrogen storage. *Nano Energy* **85**, 105989 (2021).
23. McEnaney, J. M. et al. Electrolyte engineering for efficient electrochemical nitrate reduction to ammonia on a titanium electrode. *ACS Sustain. Chem. Eng.* **8**, 2672–2681 (2020).
24. Katsounaros, I., Ipsakis, D., Polatides, C. & Kyriacou, G. Efficient electrochemical reduction of nitrate to nitrogen on tin cathode at very high cathodic potentials. *Electrochim. Acta* **52**, 1329–1338 (2006).
25. Dima, G. E., Rosca, V. & Koper, M. T. M. Role of germanium in promoting the electrocatalytic reduction of nitrate on platinum: An FTIR and DEMS study. *J. Electroanal.* **599**, 167–176 (2007).
26. Liu, M. J. et al. Catalytic performance and near-surface X-ray characterization of titanium hydride electrodes for the electrochemical nitrate reduction reaction. *J. Am. Chem. Soc.* **144**, 5739–5744 (2022).
27. Zeng, Y. et al. Surface reconstruction of water splitting electrocatalysts. *Adv. Energy Mater.* **12**, 2201713 (2022).
28. Li, S. et al. Reconstruction-induced NiCu-based catalysts towards paired electrochemical refining. *Energy Environ. Sci.* **15**, 3004–3014 (2022).
29. Zhang, M. et al. Efficient electrochemical nitrate reduction to ammonia driven by a few nanometer-confined built-In electric field. *ACS Catal.* **14**, 10437–10446 (2024).
30. Li, Y. et al. The synergistic catalysis effect on electrochemical nitrate reduction at the dual-function active sites of the heterostructure. *Energy Environ. Sci.* **17**, 4582–4593 (2024).
31. Hu, Q. et al. Designing efficient nitrate reduction electrocatalysts by identifying and optimizing active sites of Co-based spinels. *J. Am. Chem. Soc.* **146**, 2967–2976 (2024).
32. Li, J. et al. Microenvironmental corrosion and hydrolysis induced two-dimensional heterojunction of copper oxide@ferriferrous oxide for efficient electrochemical nitrate reduction to ammonia. *Chem. Eng. J.* **471**, 144488 (2023).
33. Li, X., Shen, P., Li, X., Ma, D. & Chu, K. Sub-nm RuOx clusters on Pd metallene for synergistically enhanced nitrate electroreduction to ammonia. *ACS Nano*. **17**, 1081–1090 (2023).
34. Wang, Y. et al. Enhanced nitrate-to-ammonia activity on copper–nickel alloys via tuning of intermediate adsorption. *J. Am. Chem. Soc.* **142**, 5702–5708 (2020).
35. Zhang, G., Li, X., Chen, K., Guo, Y., Ma, D. & Chu, K. Tandem electrocatalytic nitrate reduction to ammonia on MBenes. *Angew. Chem. Int. Ed.* **62**, e202300054 (2023).
36. Song, Z., Liu, Y., Zhong, Y., Guo, Q., Zeng, J. & Geng, Z. Efficient electroreduction of nitrate into ammonia at ultralow concentrations via an enrichment effect. *Adv. Mater.* **34**, 2204306 (2022).
37. Hao, R. et al. Pollution to solution: A universal electrocatalyst for reduction of all NO_x-based species to NH_3. *Chem. Catal.* **2**, 622–638 (2022).
38. Liu, H. et al. Efficient electrochemical nitrate reduction to ammonia with copper-supported rhodium cluster and single-atom catalysts. *Angew. Chem. Int. Ed.* **61**, e202202556 (2022).
39. Shit, S., Samanta, P., Bolar, S., Murmu, N. C., Khanra, P. & Kuila, T. Synthesis of iron pyrite with efficient bifunctional electrocatalytic activity towards overall water splitting in alkaline medium. *Bull. Mater. Sci.* **44**, 169 (2021).
40. Zhang R. et al. Phase engineering of high-entropy alloy for enhanced electrocatalytic nitrate reduction to ammonia. *Angew. Chemie Int. Ed.* **63**, e202407589 (2024).
41. Wang, S. et al. Interfacial polarization triggered by covalent-bonded MXene and Black phosphorus for enhanced electrochemical nitrate to ammonia conversion. *Adv. Energy Mater.* **13**, 2301136 (2023).
42. He, W. et al. Splicing the active phases of copper/cobalt-based catalysts achieves high-rate tandem electroreduction of nitrate to ammonia. *Nat. Commun.* **13**, 1129 (2022).
43. Zhu, W. et al. A hydrazine-nitrate flow battery catalyzed by a bimetallic RuCo precatalyst for wastewater purification along with simultaneous generation of ammonia and electricity. *Angew. Chem. Int. Ed.* **62**, e202300390 (2023).
44. McCrory, C. C. L., Jung, S., Peters, J. C. & Jaramillo, T. F. Benchmarking heterogeneous electrocatalysts for the oxygen evolution reaction. *J. Am. Chem. Soc.* **135**, 16977–16987 (2013).

45. Zhang, N. et al. Governing interlayer strain in bismuth nanocrystals for efficient ammonia electrosynthesis from nitrate reduction. *ACS Nano*. **16**, 4795–4804 (2022).

Acknowledgements

This work was supported by National Natural Science Foundation of China (52022037, 52202239), Taishan Scholar Project of Shandong Province (tstp20240515), Natural Science Foundation of Shandong Province (ZR2021JQ15, ZR2022QB162), Innovative Team Project of Jinan (2021GXRC019), Shandong Postdoctoral Innovation Project (SDCX-ZG-202202011), China Postdoctoral Science Foundation (2023M732037).

Author contributions

W. Zhou conceived the idea and designed the experiments. **J. Li** performed the fabrication, measurement, and analysis of the catalysts. **M. Huang** directed the experiment, and **W. Yu and H. Yuan** conducted the electrochemical measurements and data analysis. **K. Song and Y. Wang** conducted the TEM measurements. **Y. Chen, T. Wu, and D. Jiang** conducted the XAFS measurements and data analysis. **R. Hu and X. Jiang** completed the theoretical calculation analysis, and **J. Li, H. Liu, M. Huang, and W. Zhou** prepared the manuscript. All authors discussed and commented on the manuscript. **M. Huang, R. Hu, and W. Zhou** supervised the project.

Competing interests

The authors declare no competing interests.

Additional information

Supplementary information The online version contains supplementary material available at https://doi.org/10.1038/s41467-024-53833-x.

Correspondence and requests for materials should be addressed to Riming Hu, Man Huang or Weijia Zhou.

Peer review information *Nature Communications* thanks Ke Chu, Bin Zhang, Huiyuan Zhu and the other anonymous reviewer(s) for their contribution to the peer review of this work. A peer review file is available.